 doi:10.20944/preprints202009.0592.v1

Article

Mechanical Behavior of Strain-Hardening Cement-Based Composites (SHCC) Subjected to Torsional Loading and to Combined Torsional and Axial Loading

Tathiana Caram S. P. Figueiredo [a], Iurie Curosu [b,*], Giancarlo G. Gonzáles [d], Marcus Hering [c], Flávio de Andrade Silva [a], Manfred Curbach [c] and Viktor Mechtcherine [b]

[a] Department of Civil and Environmental Engineering, PUC-Rio, 22451-900, Rio de Janeiro, Brazil
[b] Institute of Construction Materials, Technische Universität Dresden, 01062, Dresden, Germany
[c] Institute of Concrete Structures, Technische Universität Dresden, 01062, Dresden, Germany
[d] Department of Mechanical Engineering, PUC-Rio, 22451-900, Rio de Janeiro, Brazil
* Correspondence: iurie.curosu@tu-dresden.de

Abstract: Strain-hardening cement-based composites (SHCC) are a novel class of fiber-reinforced concretes which exhibit high tensile strain capacity prior to failure localization. Although the tensile behavior of SHCC has been a matter of study in numerous research works, the behavior of these composites under other loading modes has scarcely been investigated. The article at hand addresses the mechanical behavior of two types of normal-strength SHCC subject to uniaxial tension, torsion, and combinations of torsional and axial loading. The SHCC under investigation were made with polyvinyl-alcohol (PVA) and ultra-high molecular weight polyethylene (UHMWPE) fibers, respectively. Digital Image Correlation (DIC) was applied to evaluate the multiple cracking process and crack opening modes in conjunction with the concretes' axial and torsional loading histories. The study demonstrates the suitability of torsion experiments to assess the multi-axial and shear performance of SHCC, highlights the relation between multiple cracking and transfer capacity for shear forces, and emphasizes the importance of the type of reinforcing fibers on the shear strength and ductility of such composites.

Keywords: SHCC; ECC; PVA fiber; UHMWPE fiber; torsion; tension; DIC

1. Introduction

Reinforced concrete (RC) structures are generally possessed of limited damage tolerance and energy dissipation capacity, traceable back to the low tensile strength and pronounced brittleness of concrete. These drawbacks can become critical under shear and torsional loading, especially when caused by intense dynamic actions [1-3]. The main risk related to such load scenarios is the sudden reduction of load-bearing capacity due to the concrete's pronounced cracking and spalling, both of which can render the steel reinforcement ineffective; see, for example, [4-6]. Furthermore, highly dynamic loading scenarios can cause failure modes different from the quasi-static ones, thereby increasing the risk of shear failure [7]. Thus, to increase the impact resilience of existing critical infrastructure there is need for appropriate strengthening solutions [8].

The application of additional layers of RC for structural strengthening has obvious disadvantages related to significant increases in the cross-sectional dimensions and in the dead weight of the structure's elements. Carbon fiber-reinforced polymers (CFRP) have been widely investigated and implemented as strengthening covers in the form of sheets [9-12] or grid-like fabrics [13-17]. Such strengthening layers are of small thickness and can considerably increase the load-bearing capacity of RC structural members. In the case of sheets, disadvantages include the

 doi:10.20944/preprints202009.0592.v1

requirement of polymeric-based adhesives, precluded observability of crack formation in the substrate, and low fire resistance. In the case of grid-reinforced strengthening layers, cracks will still start in the base element, but will propagate into the strengthening layer, usually displaying smaller widths and finer distribution. However, depending on the fiber type, grid or textile reinforcements based on continuous fibers usually exhibit brittle behavior, which impairs their resistance to shear or torsional loading. Moreover, their strengthening performance is intimately dependent on the bond with the substrate.

Strain-Hardening Cement-based Composites (SHCC), also Engineered Cementitious Composites (ECC), represent a special type of fiber-reinforced concrete with short and randomly distributed micro-fibers in volume fractions of up to 2 %. SHCC exhibit pronounced ductility prior to failure localization [18,19], while multiple cracks forming in the strain-hardening phase yield crack widths in a favorable sense less than 100 μm. These features make SHCC suitable both as main material for structural elements subject to extreme loading scenarios as well as supplementary applied retrofit and strengthening layers for enhanced structural durability and resilience under unfavorable exposure and loading conditions [20,21]. It is worthy of note that the constitutive nature and fresh-state properties of SHCC enable their application by spraying or lamination, which is an important prerequisite for structural strengthening through thin covers [22].

The remarkable crack control in SHCC leading to multiple cracking under tensile and compressive forces is responsible for the advantageous shear behavior of these composites [23]. In addition to some structural investigations on the performance of SHCC as main material [24] and for strengthening layers subject to shear [25,26], to date only a few investigations have been reported on the material characterization of SHCC under shear loading. Li *et al*. [23] investigated the shear behavior of SHCC using Ohno shear beams [27]. Although SHCC demonstrated strain-hardening and extensive deformations after the formation of the first crack, the non-uniform shear stress distribution in the middle of the beams complicated the proper characterization of shear strength. Van Zijl [28] optimized the Iosipescu beam geometry [29] and calibrated a material constitutive law employing a numerical parametric study. He found that the shear strength of SHCC exceeded its direct tensile strength by up to 50 %. However, due to the purposefully designed shape and size of the specimen, the cracked region was restricted to the notch area, impairing the load-bearing capacity and thus, obstructing the direct detection of strain-hardening behavior. Kanakubo *et al*. [30] extended the Iosipescu beam configuration by applying additional axial tensile loading. This method facilitated the analysis of the shear transfer mechanisms depending on the degree of tensile deformation but yielded results which disagreed with the results obtained by the previously quoted authors: the shear strength on a cracked surface of SHCC was reported to be about half of its tensile strength.

The wide range of reported testing methods and specimen geometries arises out of the difficulties in assuring a pure shear state in the specimen and makes comparison of different investigations unduly complex. Moreover, the experimental derivation of constitutive material laws is not trivial, requiring additional numerical simulations. Except for analytical studies in [31], no attempts have been made so far in characterizing the shear transfer mechanisms at the single-crack level in dependence on matrix composition and fiber type.

In the work reported herewith, torsion and combined torsion-tension experiments were used to characterize the multi-axial and shear behavior of two types of medium-strength SHCC. The experiments were performed under controlled loading and boundary conditions and involved four different load cases: (1) uniaxial tension; (2) torsion with blocked axial deformation; (3) torsion with free axial deformation and (4) combined torsion-tension. Optical crack monitoring of the loaded specimens with a stereo-camera system and the subsequent analysis using Digital Image Correlation (DIC) allowed a detailed characterization of the crack opening modes depending on the load case and state-of-stress in the sample. The comparative study involved SHCC made with polyvinyl-alcohol (PVA) and ultra-high molecular weight polyethylene (UHMWPE) fibers, which allowed for a clear demonstration of the influence of fiber type. Besides offering a detailed material characterization, the experimental results in this work represent a comprehensive basis for the

Preprints (www.preprints.org) | NOT PEER-REVIEWED | Posted: 25 September 2020 doi:10.20944/preprints202009.0592.v1

derivation of numerical constitutive models for SHCC subject to multi-axial loading in general and shear or torsion in particular.

2. Compositions of the SHCC under investigation and specimen fabrication

2.1. Materials

In this study, two types of SHCC were investigated. Their mixture compositions were already addressed by Curosu and Mechtcherine in previous works [40-43]. Both held the same normal-strength matrix, differing only in the type of dispersed fiber. One SHCC was made with polyvinyl alcohol (PVA) fibers produced under the brand name Kuralon REC15 (by Kuraray, Japan) [32]. The other SHCC was reinforced with UHMWPE fibers produced under the brand name Dyneema SK62 (by DSM, the Netherlands) [26]. The UHMWPE fibers will be more compactly referred to as PE in this paper, and the composites will be named according to the reinforcing fibers, i.e. PVA-SHCC and PE-SHCC, respectively. In both SHCC compositions the fiber volume fraction was 2 %. The geometric and mechanical properties of the fibers under investigation are presented in Table 1.

Table 1. Geometric and mechanical properties of PVA and PE fibers according to producers [32,33].

Fiber		**PVA**	**UHMWPE**
Diameter	[µm]	40	20
Length	[mm]	12	12
Density	[g/cm³]	1.26	0.97
Tensile strength	[MPa]	1600	2500
Young's modulus	[GPa]	40	80
Elongation at break	[%]	6.0	3.5

Despite their oil coating, the PVA fibers remain predominantly hydrophilic and form a considerable chemical bond with the cementitious matrix [34-36]. Furthermore, they exhibit relatively low abrasion resistance and pronounced slip-hardening pullout behavior, with a likely occurrence of fiber rupture at larger crack openings [37]. For this reason, the normal-strength cementitious matrix under investigation was developed specifically with respect to PVA fibers and had to ensure a limited fiber-matrix bond strength to mitigate excessive and premature fiber rupture [43]. This explains the high content of fly ash compared with the contents of cement and quartz sand; see Table 2.

In contrast, the PE fibers are hydrophobic and hence only frictionally/mechanically anchored in the matrix [38]. Furthermore, they exhibit superior tensile strength, Young's modulus, and abrasion resistance, making them especially suitable for use in high-strength cementitious matrices [39]. The crack-bridging behavior of these fibers in the normal-strength matrix was addressed in previous investigations by the authors Curosu and Mechtcherine [40-42]. Despite the relatively low bond strength in comparison to the PVA fibers, the smaller diameter of the PE fibers ensures sufficient collective crack-bridging capacity for tensile strain-hardening and multiple cracking. Furthermore, PE-SHCC is more suitable for applications involving highly dynamic loading [41,42] and when proper crack control at larger crack openings is required [40].

Table 2. Mixture compositions of the medium-strength SHCC under investigation.

	PVA-SHCC [kg/m³]	**PE-SHCC [kg/m³]**
Portland cement CEM I 42.5 R-HS (Schwenk, Germany)	505	505
Fly ash Steament H4 (Steag Power Minerals, Germany)	621	621
Quartz sand 60 – 200 µm (Strobel Quarzsand, Germany)	536	536
Water	338	333
Superplasticizer Glenium ACE 30 (BASF, Germany)	10	25
Viscosity modifying agent (SIKA, Switzerland)	4.8	4.8
PVA fiber 2 % by volume (Kuraray, Japan)	26	–
UHMWPE fiber 2 % by volume (DSM, the Netherlands)	–	20

Preprints (www.preprints.org) | NOT PEER-REVIEWED | Posted: 25 September 2020 doi:10.20944/preprints202009.0592.v1

Note that the cementitious matrices in both SHCCs are practically identical. The minor differences as shown in Table 2 are related to the slightly higher content of superplasticizer in PE-SHCC. This was required by the smaller fiber diameter of PE and the need to compensate for some decrease in workability when PE fiber is used instead of PVA fiber. Moreover, the relatively large size of the fly ash and quartz sand particles in comparison to the diameter of the PE fibers represented a drawback in terms of fiber dispersion [43]. This additionally demanded an adjustment to the mixing process, involving higher mixing energy and duration [43].

2.2. Specimen preparation

Dumbbell-shaped specimens were used in this investigation. The cross-section of the specimens in the 100 mm-long gauge portion had dimensions of 24 mm × 40 mm, the total specimen length was 250 mm, and the end sections had cross-sections of 40 mm × 40 mm; see Figure 1. This specimen geometry is not typical of torsion experiments. Previous tests showed that in the case of cylindrical specimens it is difficult to realize the tapered geometry required to confine the damage to the middle section out of the need to avoid failure initiation at the fixing locations. At the same time, besides the challenges related to specimen production, pronouncedly curved surfaces of cylindrical specimens would be disadvantageous as regards the optical monitoring of deformations and crack analysis by means of Digital Image Correlation (DIC) with the technical equipment available. Finally, the geometry chosen is common in uniaxial tension experiments for SHCC characterization [38], enabling a closer link between this program and other studies. The torsion experiments presented in this article represent the first study of this type, and they are intended to form a basis for adjustments and optimization in future works.

Batches of 3 liters were produced in each casting series of six specimens. Due to the high cohesiveness of the fresh SHCC, the specimens were not provided with a smooth top surface during production. Instead they were cast manually with a superfluous top layer, which was subsequently removed by cutting the hardened SHCC prior to testing. To avoid failure localization at the fixing locations due to stress concentrations, the specimens were additionally strengthened at their ends by embedding 50 mm-long metallic screws of 5 mm diameter during casting.

The samples were demolded 24 hours after casting, sealed in plastic sheets and stored in a curing chamber with controlled temperature of 20 °C and relative humidity of 65 %. After 14 days of curing, the specimens were prepared for testing by cutting the superfluous layers and roughening the anchorage surfaces. Because of logistical considerations, testing was performed at an average age of 65 days. At this concrete age, the hardening process can also be regarded as almost complete [44].

3. Experimental program

3.1. Testing setup and load cases

The dimensions of the dumbbell-shaped specimens with view on their tapered side are given in Figure 1. In the third direction the specimens had a constant width of 40 mm, as presented in Figure 2.

Preprints (www.preprints.org) | NOT PEER-REVIEWED | Posted: 25 September 2020 doi:10.20944/preprints202009.0592.v1

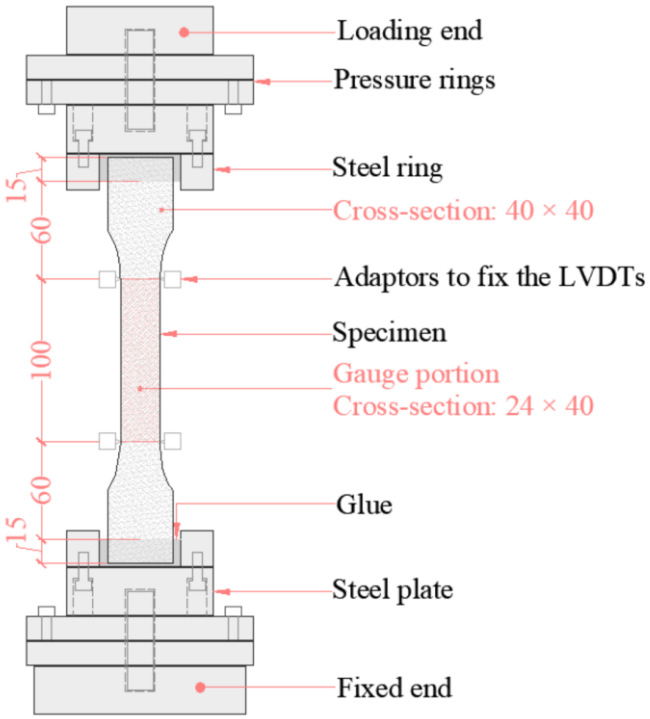

Figure 1. Specimen fixation and dimensions in mm.

The mechanical testing was performed using an Instron™ 8874 testing machine with ±25 kN axial load capacity and ±100 Nm torque capacity. The specimens were first glued at one end into a steel ring in a special frame outside the testing machine, aiming at accurate specimen alignment and centered position in the ring. After hardening of the glue, the specimen with the ring was bolted to the top, i.e., loading, assembly. By tightening four bolts in each pair of pressure rings, the assembly was pre-stressed, in this way hindering the relative sliding of the steel elements during the torsion tests. Subsequently, the sample was driven downwards into the bottom ring filled with glue; see Figure 1. A bi-component X60 glue (HBM, Germany) was used, which enabled testing after only 15 min of hardening.

In the case of the uniaxial tension experiments, the deformation of the 100 mm long gauge portion in the middle of the specimens was measured by two Linear Displacement Transducers referred as LDT (by Gefran, Italy). The LDTs had a maximum stroke of 10 mm and were attached to the specimens through a specially fabricated aluminum frame. The data acquisition system consisted of a QuantumX model MX1615B unit and a Catman DAQ software V5 (both from HBM, Germany).

Four different load cases were investigated in the presented study, as summarized in Table 3.

Table 3. Schematic representation of the load cases under investigation.

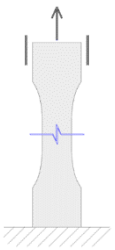	**Load case 1 (LC1):** Uniaxial tension with non-rotatable boundary conditions. Displacement-controlled mode with a displacement rate 0.05 mm/s.

Preprints (www.preprints.org) | NOT PEER-REVIEWED | Posted: 25 September 2020 doi:10.20944/preprints202009.0592.v1

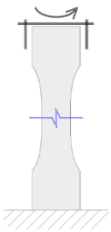	**Load case 2 (LC2):** Torsion with blocked axial deformation. Angle-controlled mode with an angular rate of 0.1 °/s. The axial compression force resulting from the hindered specimen expansion due to cracking while twisting was measured during the test.
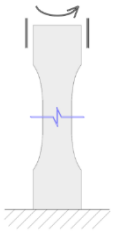	**Load case 3 (LC3):** Torsion with free axial deformation. Angle controlled mode with an angular rate of 0.1 °/s. The axial displacement was force controlled under an imposed axial force of 0 N to enable free expansion of the specimens.
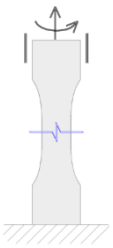	**Load case 4 (LC4):** Combined torsion and tension. Controlled axial displacement of 0.05 mm/s combined with an angle-controlled torsional loading at an angular rate of 0.1 °/s.

3.2. 3D optical measurement and DIC

A stereo system consisting of two CMOS cameras with 2.3 megapixels (Basler acA1920-155um) coupled to adjustable focal length lenses (Tamron A031 AF28-200mm F / 3.8-5.6) was used to capture images of the loaded specimens. This enabled a detailed analysis of the crack opening modes depending on loading case. The softwares VIC-Snap and VIC-3D (Correlated Solutions, USA) were used for image acquisition and analysis, respectively. The images were processed using a normalized-sum-of-squared differences (NSSD) with a subset of 21 pixels, a step of 7 pixels, and a strain window of 15 displacement points. With these parameters, the analysis provided displacement measurements with an uncertainty of approximately 0.005 %.

A speckle pattern was applied onto one of the 40 mm-wide lateral surfaces of the samples. This allowed resolving the strains and cracks in the gauge portion of the samples as illustrated in Figure 2. The global coordinate system (GCS) in the DIC analysis was positioned in the left bottom corner of the surface observed. The crack angle relative to the horizontal x-axis was derived in AutoCad (Autodesk, USA) by approximating the cracks to inclined lines.

To monitor the crack-flank displacements (CFD), virtual calipers were placed on the crack flanks, and local coordinate systems (LCS) were defined according to the crack inclination angle; cf. Figure 2. The calipers were placed parallel to the y-axis of the LCS, i.e. orthogonal to the crack. To be noted here is that the resolution of the DIC system was not sufficient to distinguish single cracks in dense crack clusters. Because of this, the distance between the digital markers u_i and v_i was 8 mm in order to include the entire width of the resolved strain bands. After the experiments, the paint was removed from the observed regions and the correct number of cracks was determined using a digital microscope VHX-6000 (Keyence, USA) with a CMOS sensor camera with 18 megapixels, providing the means accurately to interpret the crack opening values yielded by DIC. The CFD histories were evaluated in three directions as shown in Figure 2: I – normal opening, II – in-plane sliding, III – out-of-plane sliding.

Preprints (www.preprints.org) | NOT PEER-REVIEWED | Posted: 25 September 2020 doi:10.20944/preprints202009.0592.v1

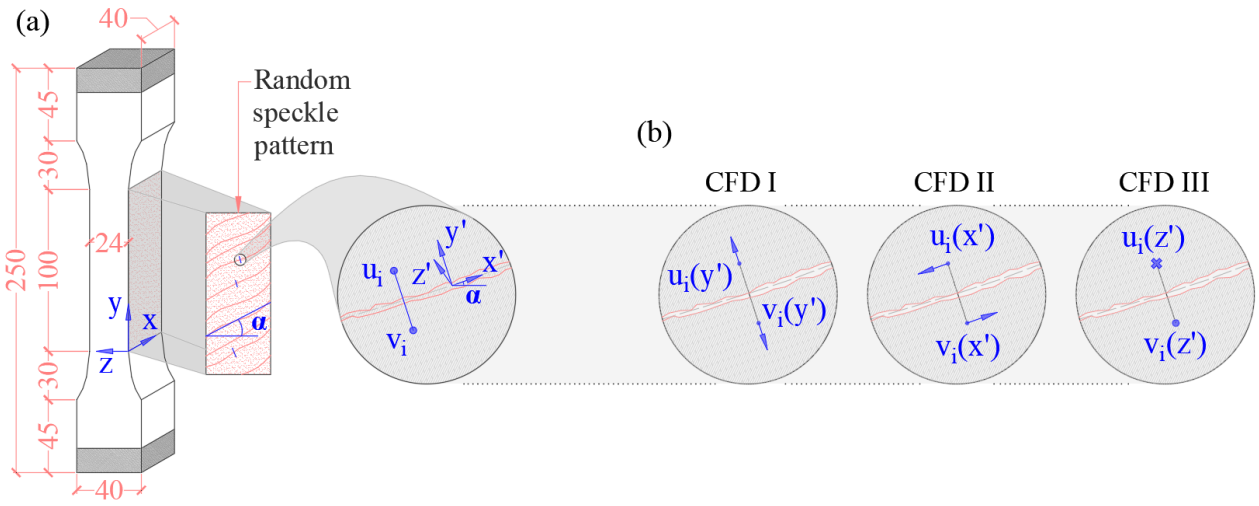

Figure 2. (a) Dumbbell-shaped specimen with dimensions in mm indicating the positions of the global (GCS) and the local coordinate systems (LCS) as well as the virtual calipers. The grey portions at the specimens' ends represent the regions embedded in the glue and encased by the metal rings. (b) Schematic representation of the assessed crack-flank displacements (CFD) in the DIC analysis.

The CFD analysis as presented in Figure 2 was not meant for the monitoring of the cracking process in the entire specimen, but to observe the relative displacement of the crack flanks of formed steady-state cracks. In the case of torsional loading, the crack-flank kinematics are determined by three components, which vary in magnitude according to the distance from the cross-sectional centroid; see Figure 3. With the given shape of the cross-section in the gauge portion, the relative magnitudes of CFD II and CFD III also depend on the position of the virtual calipers. Coming closer to the margin of the observation field CFD III should yield higher magnitudes than CFD II, while in the vicinity of the longitudinal axes of the specimen the values are negligible; see Figure 3. Thus, the virtual calipers only offer a local description of the crack flanks' displacements. To avoid data loss the virtual calipers were positioned in the quarter-span of the transverse section, with the longitudinal position varying with the availability of non-localized cracks.

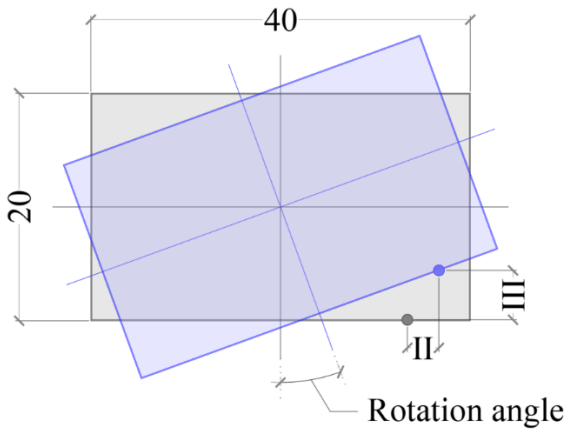

Figure 3. Schematic, exaggerated representation of the influence of cross-sectional shape in mm and location of the DIC caliper on the measured CFD II and CFD III.

4. Results and discussion

Given the multi-axial state of stress in the specimens subjected to torsion, the comparative assessment of the specimens' responses in this paper is done based on load or torque to axial deformation or rotational relationships. Note that four to five specimens were tested for each

Preprints (www.preprints.org) | NOT PEER-REVIEWED | Posted: 25 September 2020 doi:10.20944/preprints202009.0592.v1

parameter combination, but only the curves corresponding to successful tests yielding accurate material responses are presented. The discarded tests were those subject to failure in the specimen-to-glue bond, resulting in the complete pullout of the specimen from the fastening.

4.1. Uniaxial tension experiments (LC1)

Figure 4a shows the axial load-deformation curves of the SHCC under investigation, with the axial deformation (recorded as the cross-head displacement of machine) related to the total free length of the specimen, while Figure 4b shows the corresponding stress-strain curves, in which the strain applies to the 100 mm-long gauge portion. The force-displacement curves allow a direct comparison with the torsional load cases while the stress-strain curves enable the derivation of the tensile material parameters and the comparison with previous studies by the authors on identical SHCC. The tensile material parameters are summarized in Table 4.

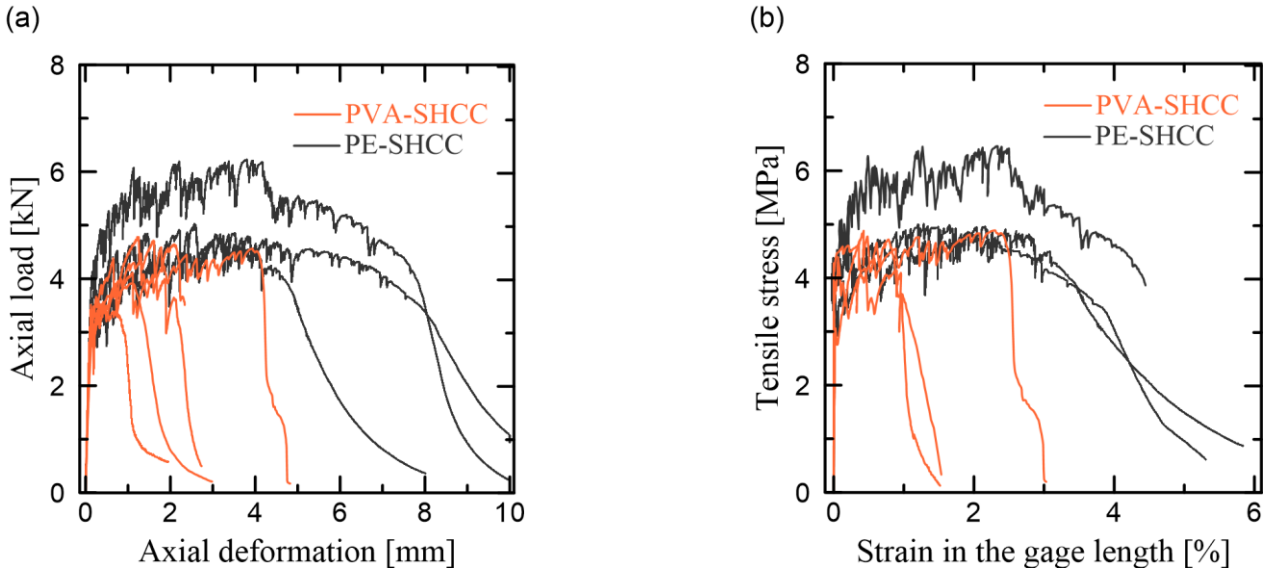

Figure 4. Uniaxial tensile behavior of PVA-SHCC and PE-SHCC: (a) load-deformation curves and (b) stress-strain curves.

Table 4. Mechanical parameters of the SHCC under uniaxial tension (LC1). Standard deviations are given in parentheses.

	σ_{1st} [MPa]	σ_{max} [MPa]	ε_{max} [%]	G_{MC} [kJ/m³]
PVA-SHCC	3.7 (0.5)	4.3 (0.5)	1.0 (0.9)	37.6 (41.1)
PE-SHCC	4.1 (0.3)	5.2 (0.7)	2.5 (0.4)	127.1 (24.6)

The average first crack stress (σ_{1st}) of PVA-SHCC was 3.7 MPa, while in the case of PE-SHCC it was 4.1 MPa. Also the tensile strength (σ_{max}) of PE-SHCC was higher than that of PVA-SHCC: 5.2 MPa vs. 4.3 MPa, respectively. Furthermore, the strain capacity (ε_{max}) up to failure localization showed considerably higher values for PE-SHCC compared to PVA-SHCC: 2.5 % vs. 1.0 %. In combination with the lower tensile strength, PVA-SHCC also yielded significantly lower work-to-fracture (G_{MC}) of 37.6 kJ/m³, which is the area under the stress-strain curves up to failure localization. PE-SHCC yielded an average work-to-fracture of 127.1 kJ/m³. These results do not completely agree with the findings of the previous studies by Curosu and Mechtcherine [40-42], in which PVA-SHCC yielded superior mechanical properties, e.g. the strain capacity of 1.5% [40]. The reason for this is likely to be the age at testing [44]. In the current work, the average age at testing was 65 days, while in the previous studies it was 14 days only. The ongoing hydration of the cementitious matrix enhanced the fiber-matrix bond strength. This had a positive effect in the case of PE-SHCC and allowed for more efficient exploitation of the high tensile strength of the PE fibers. In contrast, in the

Preprints (www.preprints.org) | NOT PEER-REVIEWED | Posted: 25 September 2020 doi:10.20944/preprints202009.0592.v1

case of PVA-SHCC, the excessive bond strength enhancement had a negative effect on the micromechanical balance leading to a pronounced fiber rupture at crack formation [45].

The different crack-bridging behavior of the fibers is also mirrored in the softening patterns of the corresponding SHCC. The steeply descending (softening) branch of the stress-strain curves for PVA-SHCC indicates fiber rupture after only limited fiber pullout, while the shallow softening of PE-SHCC suggests a lengthier fiber pullout phase. The involvement of these mechanisms was also confirmed by the visual inspection of the fracture surfaces. In the case of PVA-SHCC the protruding fibers' ends were short, at approximately 2 mm, while in the case of PE-SHCC the protruding fiber ends were longer.

The DIC evaluation was performed on several cracks for representative specimens; it indicated a significant scattering of the extent and mode of crack opening. The crack analysis presented is only valid for the representative cracks, which were neither first cracks nor localization cracks. Figure 5 presents the axial load-deformation curves along with the crack-flank displacements (CFD) histories of selected cracks in representative PVA-SHCC and PE-SHCC specimens. The CFDs were evaluated at three different load stages, as marked on the axial load-deformation curves and in the DIC images.

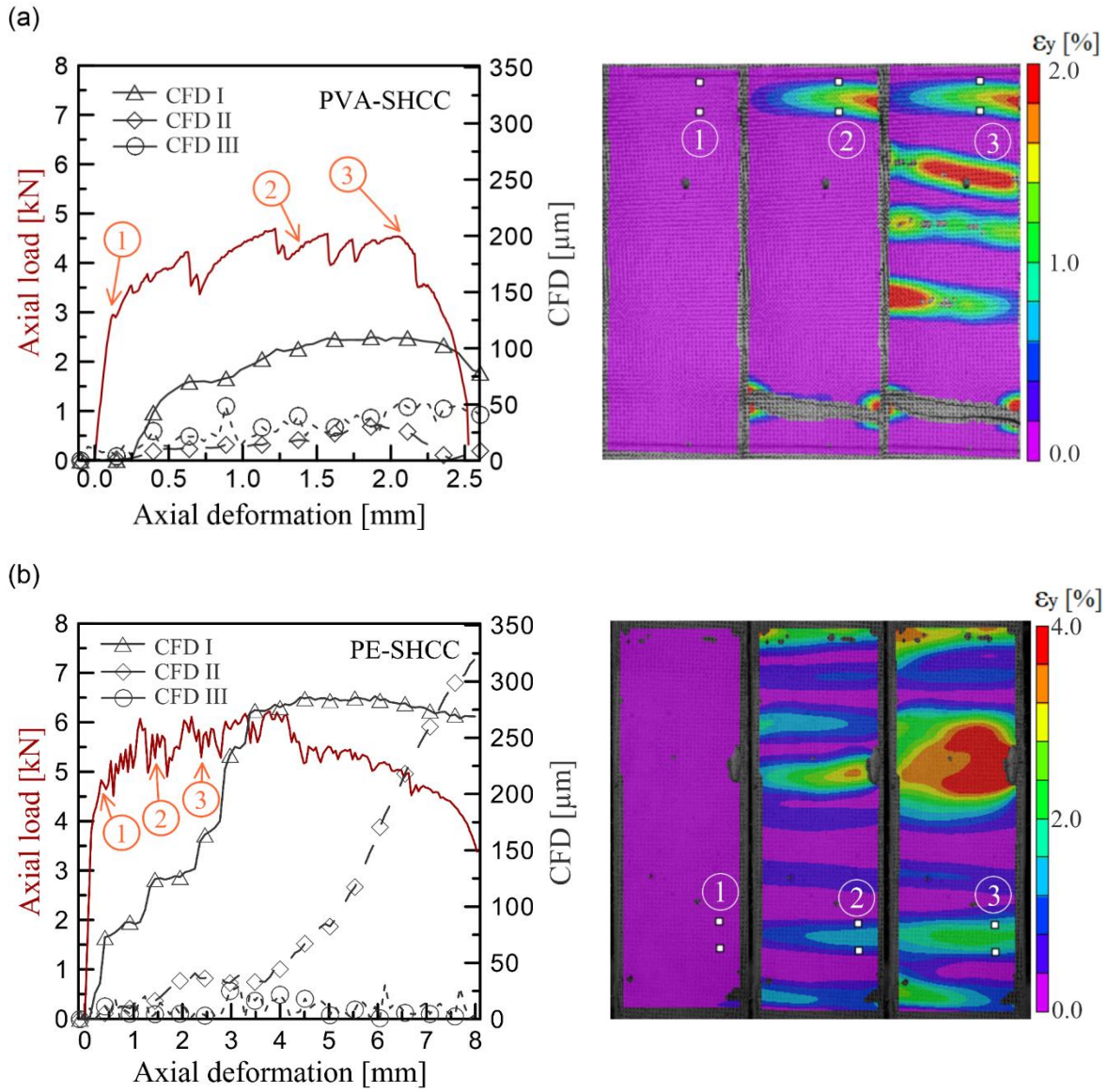

Figure 5. CFD analysis under uniaxial tension (LC1): (a) PVA-SHCC and (b) PE-SHCC. Note different x-axes (left diagrams) and different color scales (pictures on the right).

Preprints (www.preprints.org) | NOT PEER-REVIEWED | Posted: 25 September 2020 doi:10.20944/preprints202009.0592.v1

Whereas for PVA-SHCC the CFD I, i.e., normal crack opening, history shows values of about 100 μm shortly before the beginning of the softening phase, the apparent crack opening in the case of PE-SHCC reached values of 275 μm. However, the microscopic analysis of the specimen surface after the mechanical testing indicated that the PVA-SHCC specimen indeed had a single crack at the location of the virtual caliper, while in the case of PE-SHCC the strain band actually contained seven micro-cracks. The stepwise increase in CFD I in Figure 5b can be thus attributed to the successive formation of seven micro-cracks in a dense cluster. By dividing the peak CFD I value to seven cracks, the resulting average crack width is approximately 41 μm.

The average inclination angles of the cracks were 4.1° for PVA-SHCC and 5.9° for PE-SHCC. Although the CFD I histories had dominant magnitudes in both specimens, the DIC evaluation yielded significant crack-flank sliding, CFD II, defined as in-plane sliding, and III, out-of-plane sliding, in the strain-hardening phase. PE-SHCC showed a marked increase in CFD II after failure localization, despite the monitored cracks' distance from the localization crack. The crack-flank sliding can be partly traced back to the small crack inclination caused by possible specimen misalignment and the intrinsic variations of the material properties, i.e., flaws, non-uniform fiber distribution, etc. Another reason is the cracked samples' reduced stiffness, which allows specimen readjustment (rotation) and stress redistribution at the deformation stages.

It is shown in the next sections that the superior crack control and multiple cracking of PE-SHCC together with the effective crack-bridging at larger crack openings play a decisive role in the behavior of these composites under torsional loading.

4.2. Torsion experiments with blocked axial deformation (LC2)

Among the loading cases studied, LC2 simulates confined shear loading. The response of the specimens tested in LC2 is presented Figure 6. To repeat, five samples were tested per SHCC composition. The torque-rotation angle curves show the torsional resistance and the deformation capacity of the specimens depending on the type of fiber, while the compression force-rotation angle curves give a measure of the degree of axial expansion caused by matrix cracking. The experimental results of LC2 are summarized in Table 5.

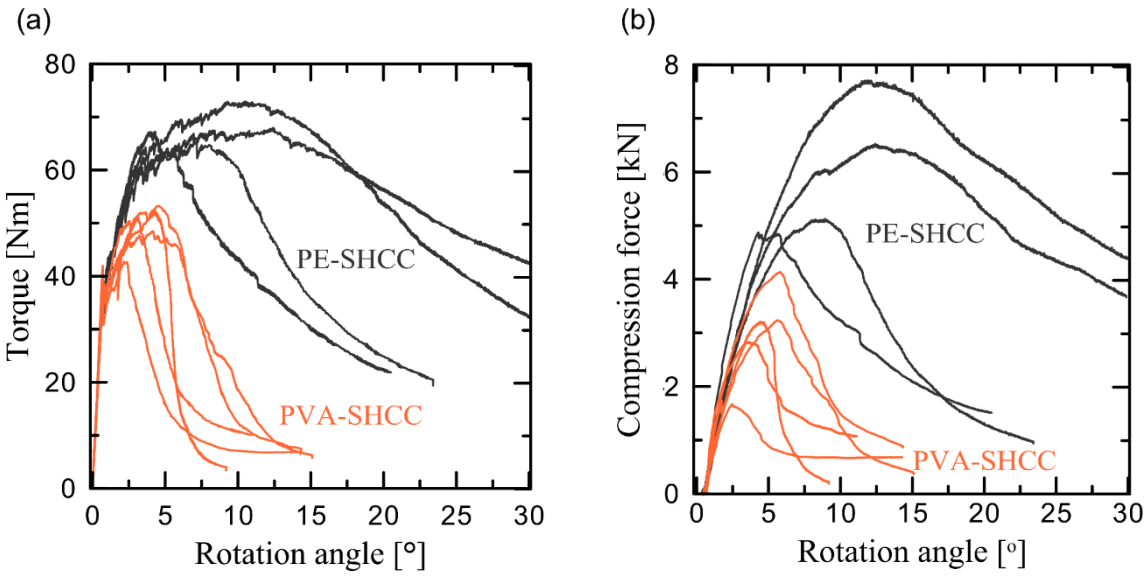

Figure 6. (a) Torque-rotation angle curves and (b) compression force-rotation angle curves obtained in torsion experiments with blocked axial deformation (LC2).

Table 5. Mechanical parameters of the SHCC under torsion with blocked axial deformation (LC2). Standard deviations are given in parentheses.

	T_{1st} [Nm]	θ_{1st} [°]	T_{max} [Nm]	$\theta_{T,max}$ [°]	F_{max} [kN]	$\theta_{F,max}$ [°]

Preprints (www.preprints.org) | NOT PEER-REVIEWED | Posted: 25 September 2020 doi:10.20944/preprints202009.0592.v1

PVA-SHCC	34.7 (4.0)	0.7 (0.1)	48.5 (4.2)	4.2 (1.0)	3.2 (0.9)	5.7 (1.4)
PE-SHCC	34.4 (2.8)	0.7 (0.0)	67.6 (3.3)	8.8 (3.6)	5.8 (1.3)	10.4 (3.7)

Although the first crack torques (T_{1st}) of the analyzed SHCC are similar, PE-SHCC yielded 39 % higher maximum torque (T_{max}) and 112 % higher rotational deformation at peak torque ($\theta_{T,max}$) than PVA-SHCC; see Table 5. Moreover, PE-SHCC yielded significantly higher angles of twist at peak torque as well as higher torsional deformations in the softening phase. The average rotation angle at peak torque was 4.2° for PVA-SHCC and 8.8° for PE-SHCC. PE-SHCC exhibited a considerably denser crack pattern with smaller crack widths, while PVA-SHCC formed few cracks with visibly larger widths.

Due to the more pronounced multiple cracking, PE-SHCC yielded more pronounced expansion and an average peak compression force of 5.8 kN, which is 81 % higher than the average value of 3.2 kN for PVA-SHCC. The compressive force in PVA-SHCC decreased rapidly in the softening phase, while in the case of PE-SHCC, it lessened slowly and even at large rotation angles showed higher values. Note that the rotation angles at maximum torque ($\theta_{T,max}$) were lower than the angles at maximum compression force ($\theta_{F,max}$). In the case of PVA-SHCC, the difference between the rotation angles at maximum torque and at peak axial compression force was 27 %, while in the case of PE-SHCC the difference was only 7 %.

Figure 7 shows the crack analysis for representative PVA-SHCC and PE-SHCC specimens. The average crack angle in the case of PVA-SHCC was 43° and in the PE-SHCC sample it was 44°. It seems that the axial compressive forces were not high enough to keep the crack inclination considerably below that of the purely torsional case, i.e. 45°. The DIC images indicate clearly the different extents of multiple cracking depending on the type of fiber. In the case of PVA-SHCC, the monitored crack showed predominantly CFD I up to peak load, with a gradual decrease in the softening phase. At the same time, CFD II and III continued increasing after failure localization. The monitored strain band actually contained two micro-cracks. By considering the CFDs at peak torque, dividing them by two cracks and summing them up, the resultant crack opening is approximately 127 µm, which is comparable to the resultant CFD in LC1.

(a)

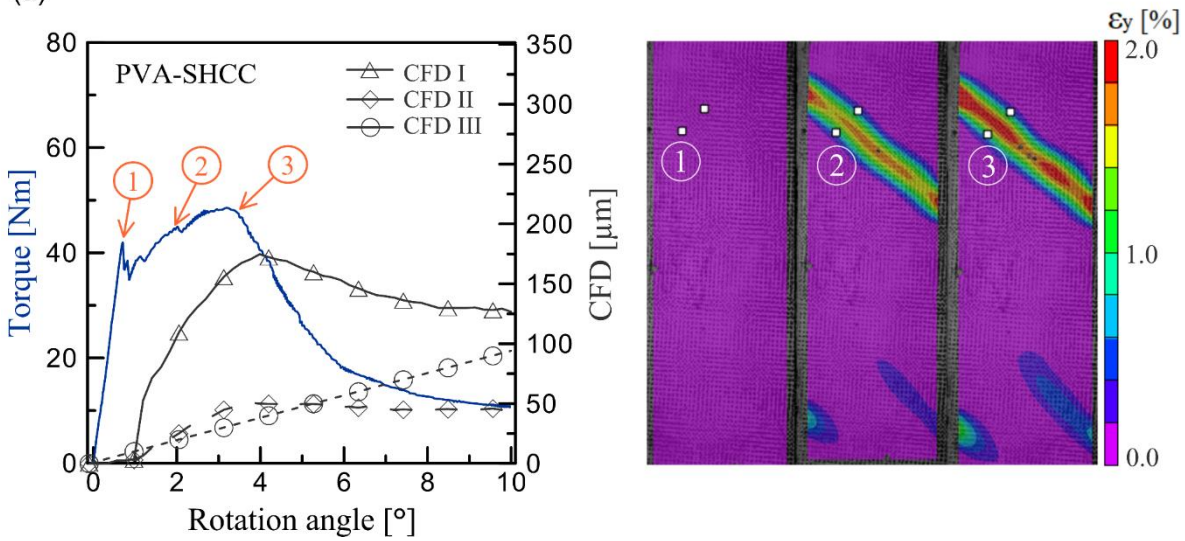

Preprints (www.preprints.org) | NOT PEER-REVIEWED | Posted: 25 September 2020 doi:10.20944/preprints202009.0592.v1

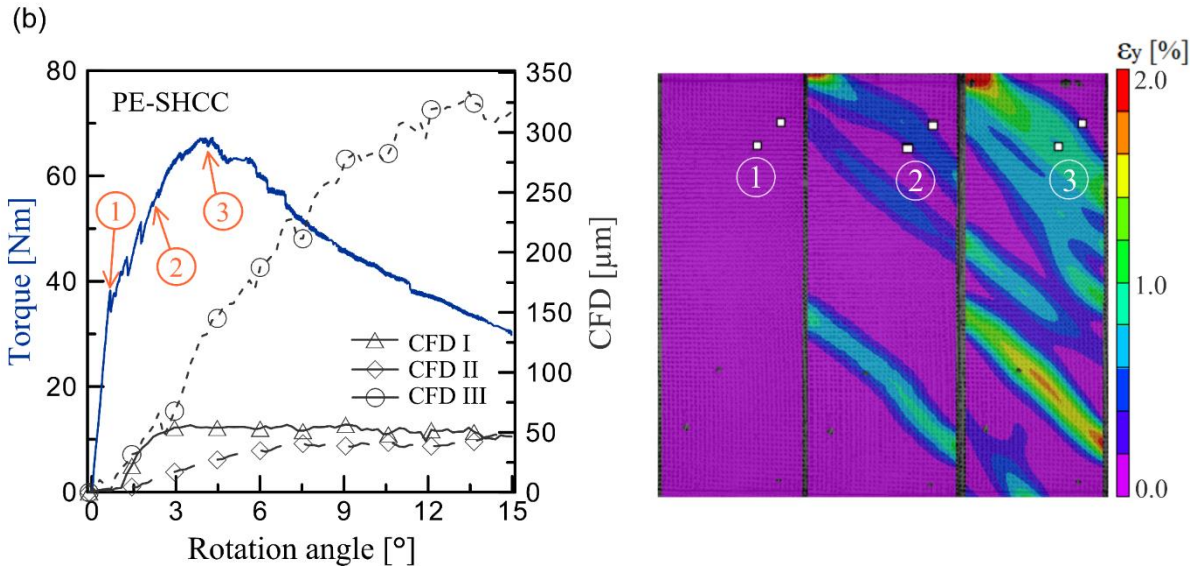

Figure 7. CFD analysis under torsion with blocked axial deformation (LC2): (a) PVA-SHCC; (b) PE-SHCC. Note the difference in the horizontal axes (left diagrams).

It can be asserted that torsional loading represents an unfavorable case with regard to steady-state cracking since the diagonal cracks propagate through a longer and more complex path compared to that in uniaxial tension experiments. Moreover, the crack openings are not uniform, and the crack-bridging capacity of the fibers is exhausted stepwise beginning at the corners. PVA-SHCC exhibits a significant drawback in this respect because its crack-bridging action vanishes completely at relatively small crack openings.

PE-SHCC yielded predominantly CFD III prior to and after peak torque, with CFD I and CFD II showing lower but similar magnitudes along the entire deformation history. The increasing width of the strain band in the DIC images clearly indicates the subsequent formation of additional micro-cracks. CFD I reaches a plateau at 50 µm prior to peak load, with no reduction during the softening phase. The magnitude of CFD I is comparable to that measured under LC1. Interestingly, the out-of-plane sliding (CFD III) continues increasing, even in the softening phase. Similar phenomena were observed under LC3 and LC4, as presented in the next sections.

Figure 8a presents a strongly deformed PE-SHCC specimen and Figure 8b shows the DIC resolved surface deformation at a rotation angle of approximately 11.3°. As opposed to PVA-SHCC, the pronounced multiple cracking in PE-SHCC facilitated a uniformly distributed deformation along the gauge portion.

Preprints (www.preprints.org) | NOT PEER-REVIEWED | Posted: 25 September 2020 doi:10.20944/preprints202009.0592.v1

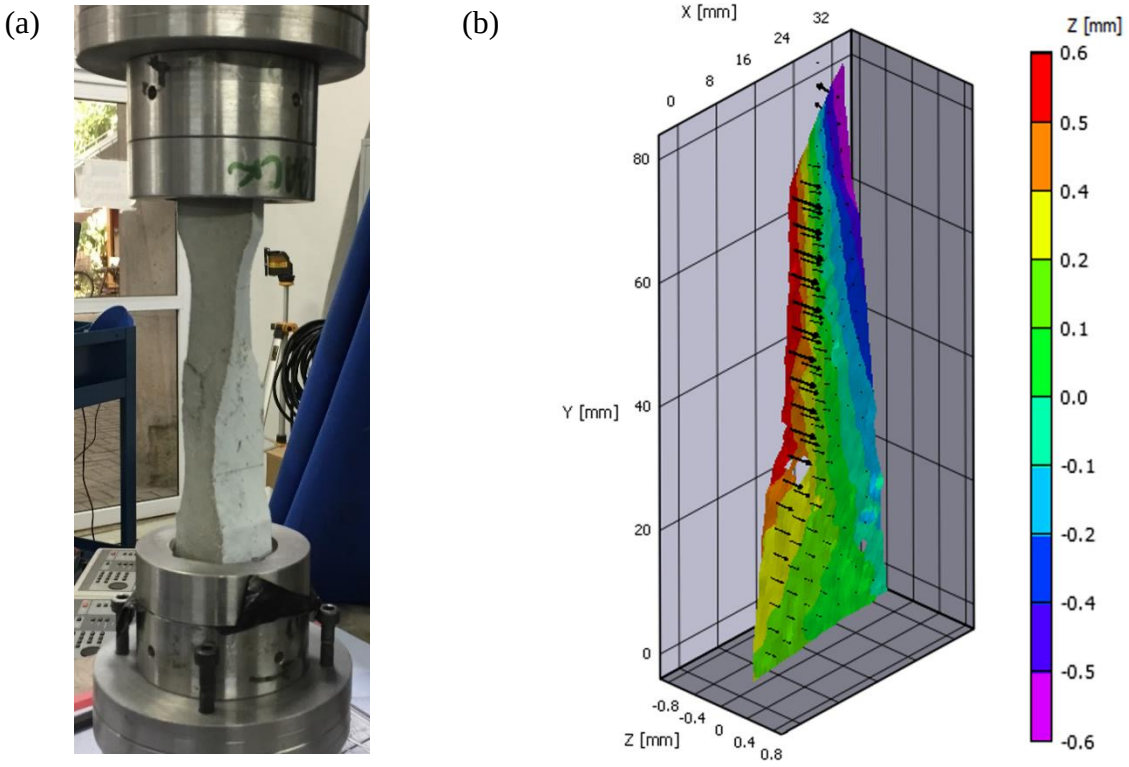

Figure 8. (a) Deformed PE-SHCC specimen and (b) 3D representation of the surface deformation at 11.3° rotation angle as resolved by DIC.

4.3. Torsion experiments with free axial deformation (LC3)

LC3 simulates an unconfined shear action. The free axial deformation of the specimens was ensured through a force controlled axial loading under imposed zero force. The behavior of the specimens subjected to LC3 is presented in Figure 9 and the experimental results are summarized in Table 6.

Except for the lower peak torque and less pronounced strain-hardening, the pattern of the torque-rotation angle curves is similar to that observed under LC2. The average values for the torque at first crack formation (T_{1st}) are also very close to those measured under LC2; see Tables 5 and 6. In the case of PVA-SHCC the maximum torque dropped just slightly from 48.5 Nm under LC2 to 45.0 Nm under LC3. For PE-SHCC the reduction in peak torque was considerably higher: 67.6 Nm for LC2 compared to 47.2 Nm under LC3. The difference can be attributed to the higher axial confinement of PE-SHCC under LC2 compared to PVA-SHCC. The rotation angles at peak torque showed a considerable drop for both SHCC from 4.2° (LC2) to 0.9° (LC3) in the case of PVA-SHCC and from 8.8° (LC2) to 5.8° (LC3) in the case of PE-SHCC.

Preprints (www.preprints.org) | NOT PEER-REVIEWED | Posted: 25 September 2020 doi:10.20944/preprints202009.0592.v1

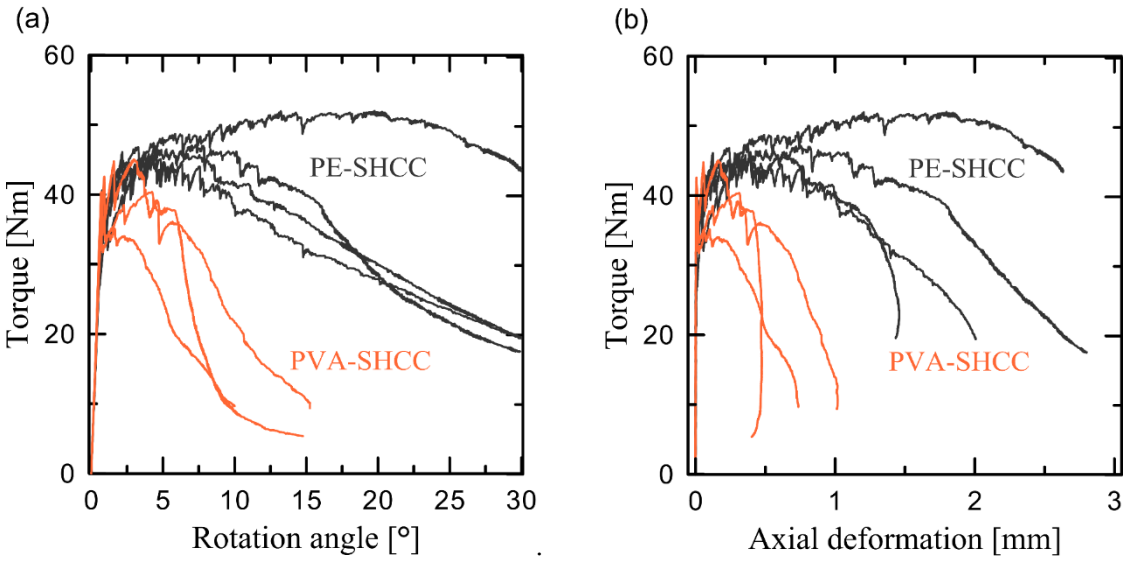

Figure 9. Mechanical behavior of PVA-SHCC and PE-SHCC under torsion with free axial deformation (LC3): (a) torque-rotation angle curves; (b) torque-axial expansion curves.

Table 6. Mechanical parameters of the SHCC under torsion with free axial deformation (LC3). Standard deviations are given in parentheses.

	T_{1st} [Nm]	θ_{1st} [°]	T_{max} [Nm]	$\theta_{T,max}$ [°]
PVA-SHCC	40.2 (1.1)	0.7 (0.1)	45.0 (2.9)	0.9 (1.3)
PE-SHCC	36.3 (5.3)	0.7 (0.2)	47.2 (2.6)	5.8 (7.9)

Figure 9b presents the axial expansion of the specimens under torsion and is in good agreement with the measured axial compression forces under LC2. Whereas the average axial deformation of PVA-SHCC prior to softening was approximately 0.1 mm, PE-SHCC showed an average deformation at peak torque higher than 0.6 mm. Considering that the multiple cracking was mostly confined in the gauge portion, this elongation represents approximately 0.6 % strain.

Under LC3 the average inclination of the cracks was 44° in the case of PVA-SHCC and 46° in the case of PE-SHCC. Seen in this way, these values are very close to the theoretical inclination of the principal stresses under pure torsion. The DIC evaluations as shown in Figure 10 indicate a dominating CFD III in the case of PVA-SHCC throughout the entire deformation history, the magnitudes of CFD I and CFD II in the pre-peak phase being considerably smaller. The dominance of CFD III is partly related to the location of the virtual calipers, as discussed above in Section 3.2. In the same fashion as under LC2, after failure localization, i.e., the softening regime, the CFD I decreased while CFD II and III increased. It can be also seen that the crack bands formed at the ends of the gauge portion, this being caused by the stress concentrations in the regions of gradual cross-section reduction.

Preprints (www.preprints.org) | NOT PEER-REVIEWED | Posted: 25 September 2020 doi:10.20944/preprints202009.0592.v1

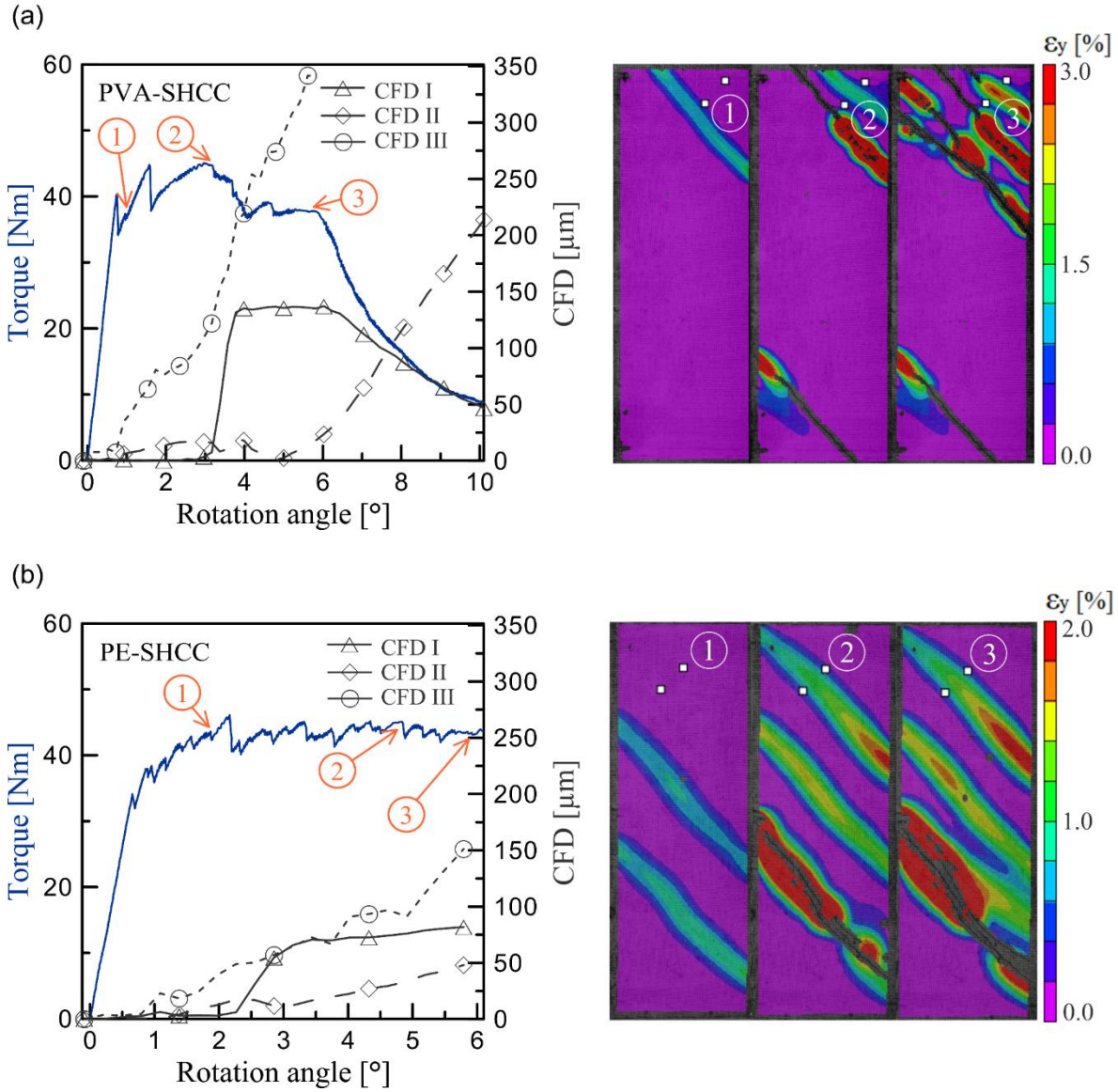

Figure 10. CFD analysis under torsion with free axial deformation (LC3): (a) PVA-SHCC; (b) PE-SHCC. Note difference in the horizontal axes (left diagrams) and color scales (pictures on the right).

In the case of PE-SHCC the resulting CFD are considerably smaller than those in PVA-SHCC. This might be a feature of the selected crack and of the position of the virtual caliper. As indicated by the color code in Figure 10b, this crack shows larger deformations closer to the edge. Also, in this case CFD III yielded dominant values, with CFD II and III occurring slightly later and showing lower magnitudes.

4.4. Combined torsion and axial tension (LC4)

Analogous to the previous load cases, the mechanical behavior of the specimens tested under combined torsion and axial tension is presented in terms of axial load-deformation and torque-rotation angle in Figure 11. A summary of the corresponding experimental results is given in Table 7. The specimens yielded average axial forces at first crack formation of 2.4 kN and 2.8 kN for SHCC made with PVA and PE fibers, respectively. This means a decrease of 32 % and 27 %, respectively, in comparison to the values measured under uniaxial tension (LC1). Furthermore, PVA-SHCC showed a reduction of 34 % in axial deformation prior to softening and 28 % reduction in peak axial load. PE-SHCC was affected to a lesser extent, exhibiting reductions of 23 % and 12 %, respectively, for these parameters; see Figure 11a.

Preprints (www.preprints.org) | NOT PEER-REVIEWED | Posted: 25 September 2020 doi:10.20944/preprints202009.0592.v1

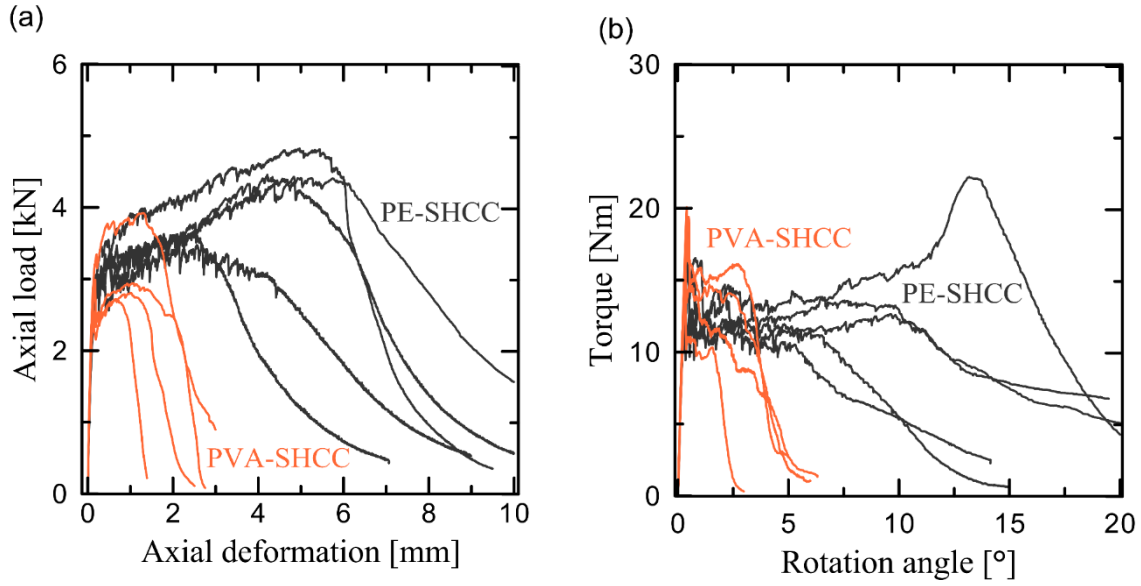

Figure 11. Behavior of the SHCC under combined torsion and tension loading (LC4): (a) axial load-deformation; (b) torque-rotation curves.

Table 7. Mechanical parameters of the SHCC under combined torsion and tension (LC4). Standard deviations are given parentheses.

	F_{1st} [MPa]	F_{max} [MPa]	T_{1st} [Nm]	θ_{1st} [°]	T_{max} [Nm]	θ_{Tmax} [°]
PVA-SHCC	2.4 (0.4)	2.9 (0.6)	17.6 (2.7)	0.5 (0.1)	12.2 (2.6)	2.4 (0.6)
PE-SHCC	2.8 (0.l)	4.4 (0.6)	13.2 (3.1)	0.3 (0.1)	12.9 (4.4)	10.0 (4.3)

The average maximum torque (prior to softening) was 12.2 Nm for PVA-SHCC and 12.9 Nm for PE-SHCC. The reduction in torsional capacity when compared with LC2 and LC3 was considerably more pronounced than that of the axial force corresponding to LC1. This may possibly be related to the strains in the axial direction dominating over those in the transversal direction, as defined by the axial displacement rate of 0.05 mm/s and angular rate of 0.1 °/s. Although the CFD analysis provided some evidence in this respect, numerical simulations would be needed for a more reliable estimation of the principal stresses corresponding to the imposed displacement/angular rates.

The combined loading (LC4) resulted in intermediary values for the average crack angle, i.e. between those obtained for LC1 and LC3. The average crack inclination angles were 33 % for PVA-SHCC and 27 % for PE-SHCC. Similar to the other load cases, PVA-SHCC showed broader scattering among the CFDs of different cracks, while crack localization occurred even more rapidly. The crack monitored in the case of PVA-SHCC yielded a dominating CFD II sliding with a value of approximately 200 μm at the initiation of softening. During the softening phase, CFD II continued increasing while CFD I and II showed elastic recovery. In contrast, CFD I was dominant throughout the deformation history of PE-SHCC, whereas CFD III increased only after failure localization.

Preprints (www.preprints.org) | NOT PEER-REVIEWED | Posted: 25 September 2020 doi:10.20944/preprints202009.0592.v1

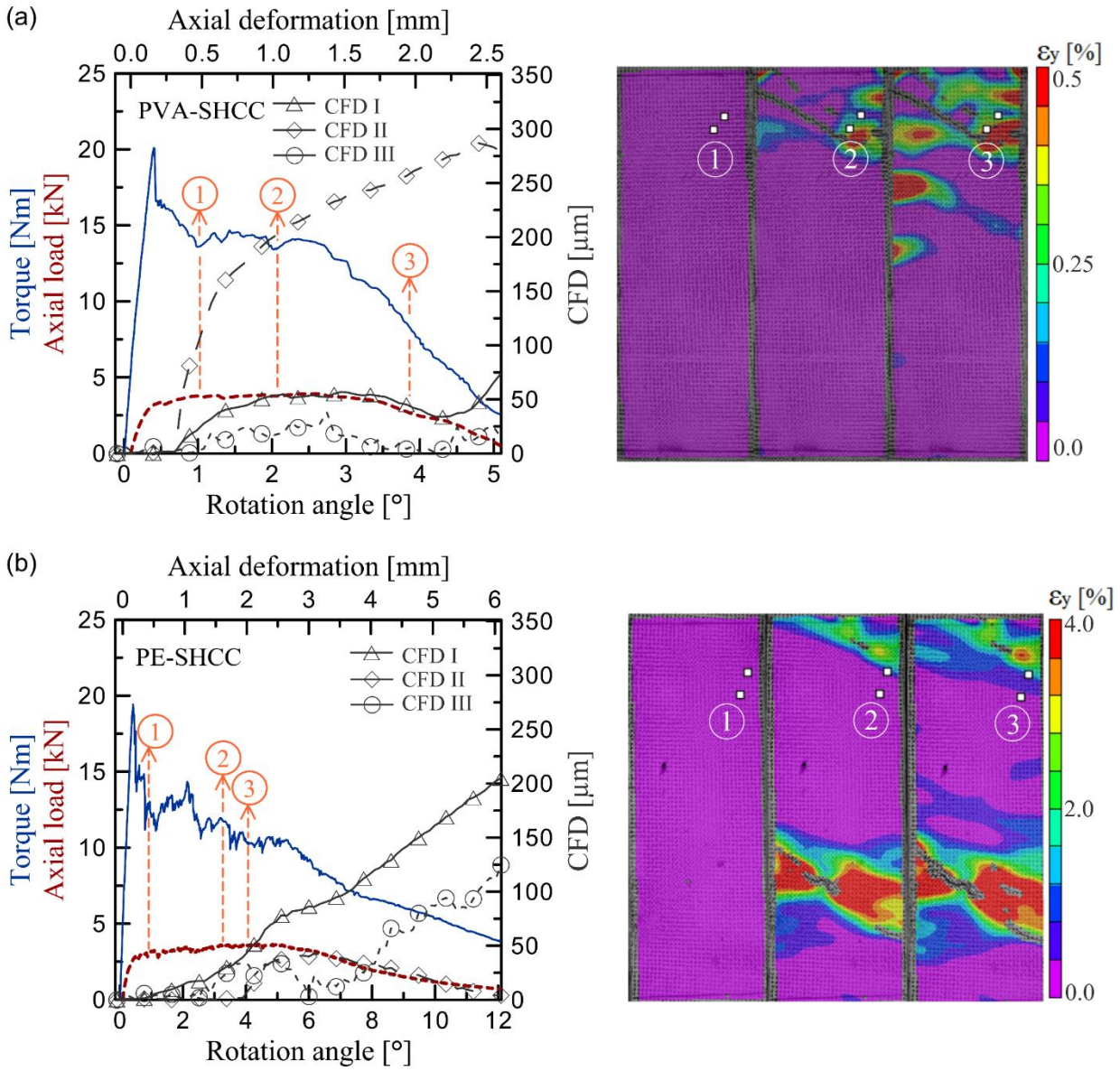

Figure 12. CFD-analysis of the specimens tested under combined torsion and tension loading (LC4): (a) PVA-SHCC; (b) PE-SHCC. Note different axes (left diagrams) and different color scales (pictures on the right).

4.5. Concluding comparison of all load cases

A generalized comparison of the material response under LC1 and LC4 is presented in Figure 13 through the envelopes of the load-deformation curves of PVA-SHCC and PE-SHCC, respectively. The axial tensile strength and ductility decreased for both composites when the loading mode changed from the uniaxial tension (LC1) to the combined tension-torsion regime (LC4). However, PVA-SHCC yielded a considerably more significant reduction, especially in axial deformation.

Preprints (www.preprints.org) | NOT PEER-REVIEWED | Posted: 25 September 2020 doi:10.20944/preprints202009.0592.v1

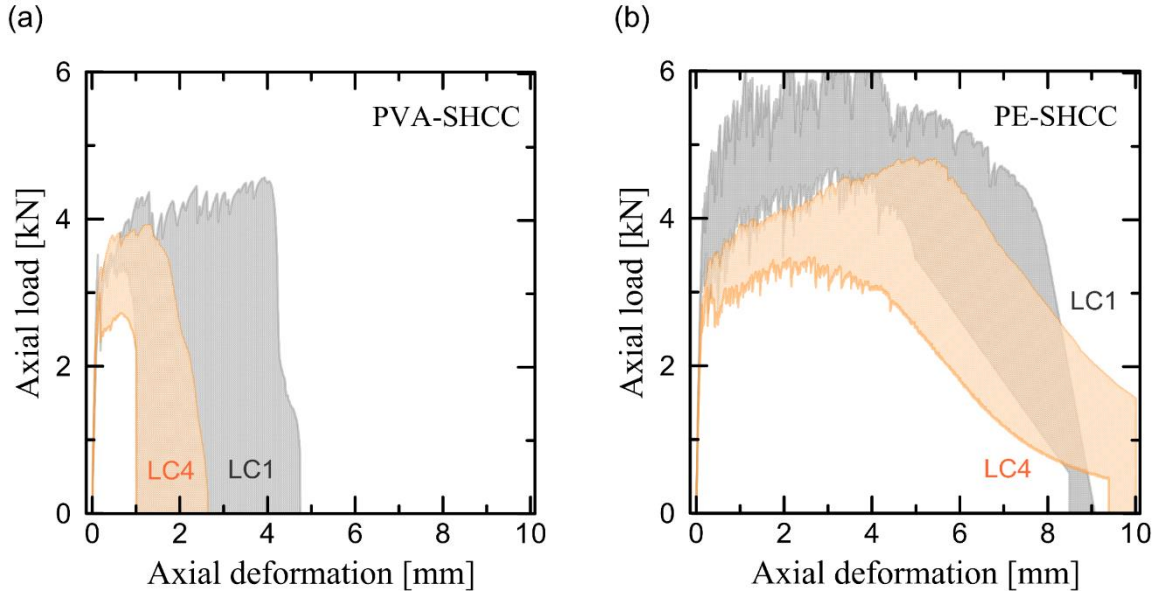

Figure 13. Envelopes of the axial load-deformation curves under LC1 (uniaxial tension) and LC4 (combined tension and torsion): (a) PVA-SHCC and (b) PE-SHCC.

Figure 14 presents a general overview of the material response under the torsional load cases through the envelopes of the torque-rotation angle curves. Both SHCC compositions yielded the highest load-bearing capacity and deformability up to peak load under LC2, while under LC3 they showed shallower softening branches compared to LC2. Finally, the combination of tensile and torsion forces (LC4) induced a dramatic reduction in torsional resistance. However, this can be partly traced back to the axial displacement rate's being higher than the angular one. In comparison to the other load cases, the combined loading LC4 contributed to the localization of the cracks while reducing the pseudo-interlock generated not by the aggregates, which are finely graded, but by the cracked surfaces, thus reducing the overall energy absorption capacity in this configuration. An indication of the dominance of this effect is shown in Figure 13, with the reduction in the axial load bearing capacity much less pronounced.

Regarding the performance of SHCC under shear, the adopted setup holds large potential, providing not only the shear strength, focus of previous studies [23,28,30], but enabling a unconditioned full-field strain evaluation, due to the absence of stress concentration elements (e.g. notches). Moreover, the system enabled the SHCC specimens to develop the multiple-cracking process until the complete depletion of load-bearing capacity due to the absence of auxiliary loads in the gage length, providing a reliable response of the material behavior even in the softening phase. With the four loading cases, important data is provided for eventual numerical studies related to SHCC performance. Even though the single-crack response could not be fully assessed due to limitations in the resolution of the available equipment, the obtained quantitative and qualitative data on the behavior of SHCC under various loading conditions serves as detailed input for calibrating material laws in numerical simulations.

Preprints (www.preprints.org) | NOT PEER-REVIEWED | Posted: 25 September 2020 doi:10.20944/preprints202009.0592.v1

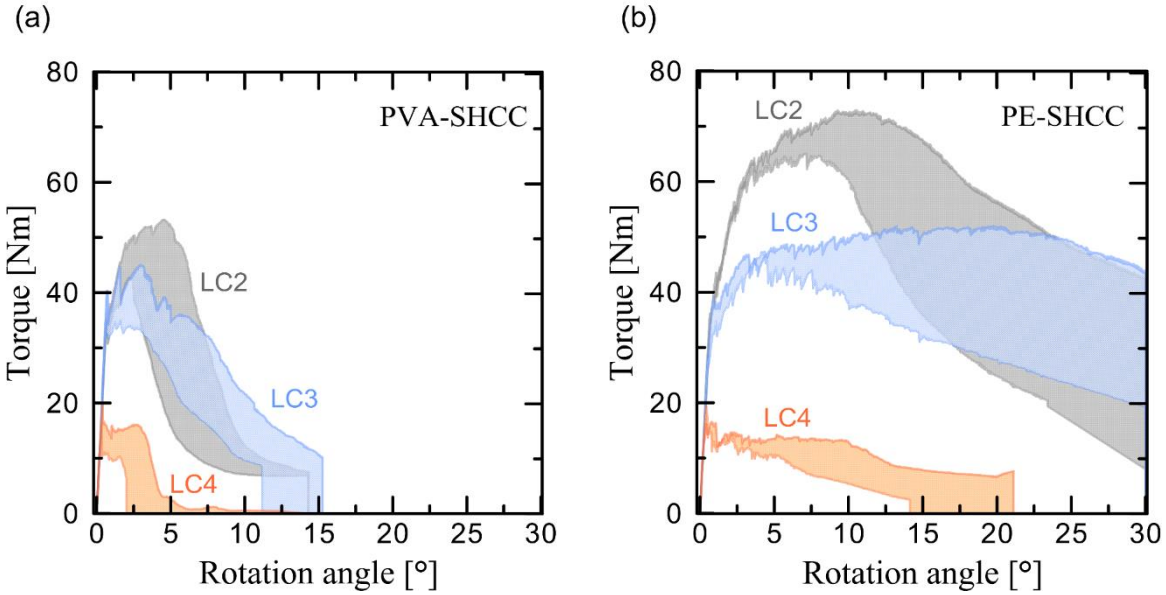

Figure 14. Influence of load case on the torsional response of (a) PVA-SHCC and (b) PE-SHCC.

With respect to the fibers, the experimental results demonstrate that PE-SHCC yield superior mechanical properties compared to PVA under all load cases. Whereas the pre-peak crack-bridging behavior of the PE fibers ensures more pronounced multiple cracking compared to PVA-SHCC, the post-peak, i.e., softening, crack-bridging action ensures considerable stress transfer even at large crack openings, which contributes to higher torsional load-bearing capacity and ductility; see Figure 15. At the same time, the slip-hardening behavior of the PVA fibers affects not just the uniaxial tensile properties of PVA-SHCC but leads to a more pronounced reduction in mechanical performance under combined loading conditions.

Preprints (www.preprints.org) | NOT PEER-REVIEWED | Posted: 25 September 2020 doi:10.20944/preprints202009.0592.v1

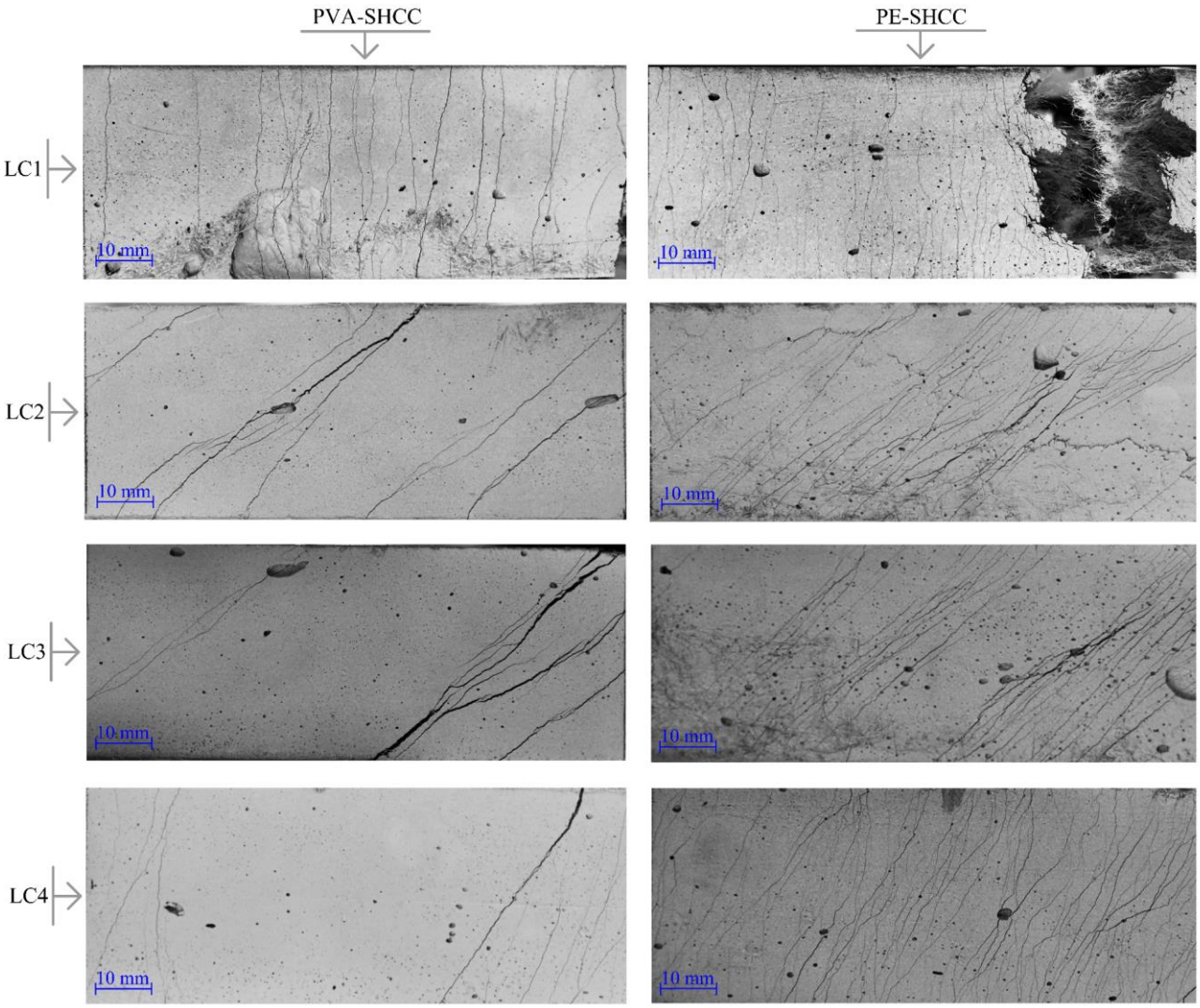

Figure 15. Failure cracking patterns of representative specimens in each load case.

5. Conclusions and outlook

The paper presents the results of an extensive experimental study on the mechanical behavior of two types of normal-strength SHCC under four different load cases: uniaxial tension, torsion with blocked axial deformation, torsion with free axial deformation and combined tension-torsion. The difference in the analyzed SHCC consisted in the reinforcing fibers, which were made of PVA and UHMWPE, respectively.

It was shown that the SHCC made with UHMWPE fibers (PE-SHCC) demonstrated superior behavior under all load cases compared to the SHCC made with PVA fibers (PVA-SHCC). This was traced back to the superior pre-peak and post-peak crack-bridging behavior of the UHMWPE fibers. The slip-hardening pullout behavior of PVA and the resulting fiber rupture at small crack openings resulted in inferior multiple cracking of PVA-SHCC under uniaxial tensile loading and in a pronounced negative effect of torsional and multi-axial loading.

Both types of SHCC yielded substantial axial expansion under torsion, the expansion being proportional to the degree of multiple cracking. The axial confinement of the specimens subject to torsion resulted in a higher torsional load bearing capacity, but also in a more abrupt softening phase in comparison to the specimens also subject to torsion but with free axial deformation. Finally, the combined tension-torsional loading led to a dramatic reduction in torsional strength and deformability of both SHCC. However, the latter was partly attributed to the applied axial displacement rate, which seemed to dominate the angular rate.

The cracking process and the crack-flank kinematics in SHCC under various loading conditions were monitored with the help of a stereo camera system and quantitatively analyzed by means of DIC. Despite the detailed information on crack-flank displacements, the pronounced variation of the latter among various cracks in individual specimens did not allow quantification of the shear-transfer capacity in dependence on crack opening mode and magnitude. It may be assumed that the involvement of shorter samples and the purposeful integration of inclined notches would enable a restriction of the crack formation to the notched region and a more detailed crack analysis. This will be a matter of interest in future studies.

In an upcoming study, the SHCC presented in this paper is to be investigated in application as shear-strengthening layers on impacted beams. The experiments on a structural scale will be complemented by numerical simulations and the results presented in the paper at hand will serve as experimental basis for calibrating material laws for SHCC in the numerical models.

Acknowledgments: The authors would like to express their gratitude to the Technical Manager of the *Instituto Tecnológico,* M.Sc. Adrian Giassone, for his invaluable support. Additionally, this study was financed in part by the *Coordenação de Aperfeiçoamento de Pessoal de Nível Superior* CAPES (Brazil) - Finance Code 001. Moreover, support by CAPES (Brazil) through the Probral program Nº12/2017 and DAAD (Germany) within the research project 8887.144079/2017-00 is gratefully acknowledged. The 1st author also expresses gratitude to the Brazilian Agency CNPq for her stipend. Finally, the authors at the TU Dresden appreciate the funding by the *Deutsche Forschungsgemeinschaft* (DFG - German Research Foundation) in the framework of the Research Training Group GRK 2250/1 "Mineral-bonded composites for enhanced structural impact safety", project number 287321140.

Data availability: The raw/processed data required to reproduce these findings cannot be shared at this time as the data also form part of an ongoing study.

References

[1] Paulay, T. 1997. Displacement-based design approach to earthquake-induced torsion in ductile buildings. *Engineering Structures* 19(9): 699-707.

[2] Tachibana, S., Masuya, H., Nakamura, S. 2010. Performance based design of reinforced concrete beams under impact. *Natural Hazards and Earth System Science* 10: 1069-1078.

[3] Ren, Q. X., Han, L. H., Hou, C., Tao, Z., Li, S. 2017. Concrete-encased CFST columns under combined compression and torsion: Experimental investigation. *Journal of Constructional Steel Research* 138: 729-741.

[4] Kühn, T., Hering, M., Häußler-Combe, U., Curbach, M. 2018. Dynamic behaviour of reinforced slabs – blast testing. Proceedings of the 5th International Conference on Protective Structures, Poznan, Poland, 2018, 9 pages.

[5] Aoude, H., Dagenais, F. P., Burrell, R. P., Saatcioglu, M. 2015. Behavior of ultra-high performance fiber reinforced concrete columns under blast loading. *International Journal of Impact Engineering* 80: 185-202.

[6] Yoo, D.-Y., Banthia, N. 2019. Impact resistance of fiber-reinforced concrete – A review. *Cement and Concrete Composites* 104: 103389. https://doi.org/10.1016/j.cemconcomp.2019.103389.

[7] Saatci, S., Vecchio, F. J. 2009. Effects of shear mechanisms on impact behavior of reinforced concrete beams. *ACI Structural Journal* 106(1): 78-86.

[8] Goswami, A., Adhikary, S. Das, A. 2019. Retrofitting materials for enhanced blast performance of Structures: Recent advancement and challenges ahead. *Construction and Building Materials* 204: 224-243.

[9] Ghobarah, A., Ghorbel, M. N., Chidiac, S. E. 2002. Upgrading torsional resistance of reinforced concrete beams using fiber-reinforced polymer. *Journal of Composites for Construction* 6: 257-263.

[10] Ameli, M., Ronagh, H., Dux, P. 2007. Behavior of FRP Strengthened Reinforced Concrete Beams under Torsion. *Journal of Composites for Construction* 11(2): 192-200.

[11] Chalioris, C.E. 2008. Torsional strengthening of rectangular and flanged beams using carbon fibre-reinforced-polymers – Experimental study. *Construction and Building Materials* 22: 21-29.

[12] Nikoloutsopoulos, N., Passa, D., Gavela, S., Sotiropoulou, A. 2018. Comparison of shear strengthening techniques of reinforced concrete beams with carbon fibre reinforced polymers (CFRPs). *Procedia Structural Integrity* 10: 141-147.

[13] Schladitz, F., Curbach, M. 2012. Torsion tests on textile-reinforced concrete strengthened specimens. *Materials and Structures* 45: 31-40. DOI: 10.1617/s11527-011-9746-5.

[14] Brückner, A., Ortlepp, R., Curbach, M. 2006. Textile Reinforced Concrete for Strengthening in Bending and Shear. *Materials and Structures* 39: 741-748. DOI: 10.1617/s11527-005-9027-2.

[15] Tetta, Z. C., Koutas, L. N., Bournas, D. A. 2015. Textile-reinforced mortar (TRM) versus fibre-reinforced polymers (FRP) in shear strengthening of concrete beams. *Compos. Part B: Eng.*77: 338–348. https://doi.org/10.1016/j.compositesb.2015.03.055.

[16] Loreto, G., Babaeidarabad, S., Leardini, L., Nanni, A. 2015. RC beams shear-strengthened with fabric-reinforced-cementitious-matrix (FRCM)composite. *Int. J. Adv. Struct. Eng.*7 (4): 341–352. https://doi.org/10.1007/s40091-015-0102-9.

[17] Alabdulhady, M. Y., L. H. Sneed, and C. Carloni. 2017. Torsional behaviour of RC beams strengthened with PBO-FRCM composite – An experimental study. *Eng. Struct*. 136: 393–405. https://doi.org/10.1016/j.engstruct.2017.01.044.

[18] Toshiyuki, K., Kabele, P., Fukuyama, H., Uchida, Y., Suwada, H., Slowik, V. 2012. Strain Hardening Cement Composites: Structural Design and Performance: State-of-the-Art Report of the RILEM Technical Committee 208-HFC, SC3. Springer Science & Business Media. 90 pages.

[19] Li, V. C. 2003. On Engineered Cementitious Composites (ECC) – A review of the material and its applications. *Journal of Advanced Concrete Technology* 1(3): 215-230.

[20] Mechtcherine, V. (2013). Novel cement-based composites for the strengthening and repair of concrete structures. *Construction and Building Materials* 41: 365-373 DOI: 10.1016/j.conbuildmat.2012.11.117 .

[21] Khalil, A. E. H., Etman, E., Atta, A., Essam, M. 2017. Behavior of RC beams strengthened with strain hardening cementitious composites (SHCC) subjected to monotonic and repeated loads. *Engineering Structures* 140: 151-163.

[22] Huang, B. T., Li, Q. H., Xu, S. L., Zhou, B. 2019. Strengthening of reinforced concrete structure using sprayable fiber-reinforced cementitious composites with high ductility. *Composite Structures* 220: 940-952.

[23] Li, V., Mishra, D., Naaman, A., Wight, J., LaFave, J. M., Wu, H. C, Inada, Y. 1994. On the shear behavior of engineered cementitious composites. *Advanced Cement Based Materials*: 142-149.

[24] Yin, L., Yan, C., Liu, S., Zhang J., Liang, M. 2019. Shear behavior of a strain hardening cementitious composites (SHCC)-Grooved steel composite deck. *Composites Part B: Engineering* 160: 195-204.

[25] Wang, G., Yang, C., Pan, Y., Zhu, F., Jin, K., Li, K., Nanni, A. 2019. Shear behaviors of RC beams externally strengthened with engineered cementitious. *Materials* 12(13): 2163, 16 pages. DOI: 10.3390/ma12132163.

[26] Wei, J., Chen, Y., Wu, C., Leung, C. K. Y. 2019. Shear strengthening of reinforced concrete beams with high strength strain-hardening cementitious composites (HS-SHCC). In: Pijaudier-Cabot *et al*. (eds.): Proc. of 10th International Conference on Fracture Mechanics of Concrete and Concrete Structures FraMCoS-X, Bayonne, France 23-26 June, 2019, 9 pages. DOI: 10.21012/FC10.233281.

[27] Arakawa, T., Ono, K. 1957. Shear tests of reinforced concrete beams by special type of loading (in Japanese). *Transactions of the Architectural Institute of Japan* 57: 581-584.

[28] Van Zijl, G. P. A. G. 2007. Improved mechanical performance: Shear behavior of strain-hardening cement-based composites (SHCC). *Cement and Concrete Research* 37: 1241-1247.

[29] Iosipescu, N. 1967. New accurate method for single shear testing of metals. Journal of Materials 2(3): 537-566.

[30] Kanakubo, T., Shimizu, K., Nagai, S., Kanda, T. 2010. Shear transmission on crack surface of ECC. In: Oh, B. H. *et al*. (Eds.): Fracture mechanics of concrete and concrete structures – Proc. of FraMCoS-7, Jeju (South Korea). pp. 1623-1630.

[31] Wu, C., Leung, C. K. Y., Li, V. C. 2018. Derivation of crack bridging stresses in engineered cementitious composites under combined opening and shear displacements. *Cement and Concrete Research* 107: 253-263.

[32] Kuraray Co. Ltd. 2018. Kuralon K II high tenacity type fibers. http://www.kuraray.co.jp/kii/english/ (accessed January, 2020).

[33] Fact Sheet, Ultra High Molecular Weight Polyethylene fiber from DSM Dyneema, Eurofibers, (2012). https://issuu.com/eurofibers/docs/name8f0d44 (accessed January 9, 2020).

[34] Kanda, T., Li, V. C. 1998. Interface property and apparent strength of high-strength hydrophilic fiber in cement matrix. *Journal of Materials in Civil Engineering* 10(1): 5-13.

[35] Li, V. C., Wu, C., Wang, S., Ogawa, A., Saito, T. 2002. Interface tailoring for strain-hardening polyvinyl alcohol-engineered cementitious composite (PVA-ECC). *ACI Materials Journal* 99(5): 463-472.

[36] Arain, M. F., Wang, M., Chen, J., Zhang, H. 2019. Experimental and numerical study on tensile behavior of surface modified PVA fiber reinforced strain-hardening cementitious composites (PVA-SHCC). *Construction and Building Materials* 217: 403-415.

[37] Ranjbarian, M., Mechtcherine, V., Zhang, Z., Curosu, I., Storm, J., Kaliske, M. 2019. Locking front model for pull-out behavior of PVA microfibre embedded in cementitious matrix. *Cement and Concrete Composites* 103: 318-330.

[38] Curosu, I., Liebscher, M., Mechtcherine, V., Bellmann, C., Michel, S. 2017. Tensile behavior of high-strength strain-hardening cement-based composites (HS-SHCC) made with high-performance polyethylene, aramid and PBO fibers. *Cement and Concrete Research* 98: 71-81.

[39] Ranade, R., Li, V. C., Stults, M. C., Rushing, T. S., Roth, J., Heard, W. F. 2013. Micromechanics of high-strength, high-ductility concrete. *ACI Materials Journal* 110 (4): 375-384.

[40] Curosu, I., Pirskawetz, S., Mechtcherine, V. 2015. Characterizing the crack development in strain-hardening cement-based composites (SHCC) by means of acoustic emission. In: Saouma, V., Bolander, J., Landis, E. (eds) 9th International Conference on Fracture Mechanics of Concrete and Concrete Structures FraMCoS-9, Berkeley, California, USA.

[41] Curosu, I., Mechtcherine, V., Millon, O. 2016. Effect of fiber properties and matrix composition on the tensile behavior of Strain-Hardening Cement-Based Composites (SHCCs) subject to impact loading. *Cement and Concrete Research* 82: 23-35.

[42] Curosu, I., Mechtcherine, V., Forni, D., Cadoni, E. 2017. Performance of various strain-hardening cement-based composites (SHCC) subject to uniaxial impact tensile loading. *Cement and Concrete Research* 102: 16-28.

[43] Curosu, I. 2018. Influence of fiber type and matrix composition on the tensile behavior of strain-hardening cement-based composites (SHCC) under impact loading. Doctoral thesis. Schriftenreihe des Instituts für Baustoffe Heft 2018/1, V. Mechtcherine (Ed.), TU Dresden.

[44] Klink, T., Stegmann, F., Slowik, V. 2019. Age dependence of cracking and deformability of a strain-hardening cement-based composite. *Construction and Building Materials* 214: 641-647.

[45] Li, V. C., Leung, C. K. Y. 1992. Steady-state and multiple cracking of short random fiber composites. *Journal of Engineering Mechanics* 118: 2246-2264.